There is a super-Chandrasekhar mass type Ia supernova progenitor located 49 pc away that will detonate in 23 Gyr

James Munday,[1]★ Ruediger Pakmor,[2] Ingrid Pelisoli,[1] David Jones,[3,4,5] Snehaleta Sahu,[1] Pier-Emmanuel Tremblay,[1] Abinaya Swaruba Rajamuthukumar,[2] Gijs Nelemans,[6,7,8] Mark Magee,[1] Silvia Toonen,[9] Antoine Bédard,[1] Tim Cunningham[10]

[1] *Department of Physics, Gibbet Hill Road, University of Warwick, Coventry CV4 7AL, United Kingdom*
[2] *Max-Planck-Institut für Astrophysik, Karl-Schwarzschild-Str. 1, D-85748, Garching, Germany*
[3] *Instituto de Astrofísica de Canarias, E-38205 La Laguna, Tenerife, Spain*
[4] *Departamento de Astrofísica, Universidad de La Laguna, E-38206*
[5] *Nordic Optical Telescope, Rambla José Ana Fernández Pérez*
[6] *Department of Astrophysics/IMAPP, Radboud University, P.O. Box 9010, 6500 GL Nijmegen, The Netherlands*
[7] *Institute for Astronomy, KU Leuven, Celestijnenlaan 200D, 3001 Leuven, Belgium*
[8] *SRON, Netherlands Institute for Space Research, Niels Bohrweg 4, 2333 CA Leiden, The Netherlands*
[9] *Anton Pannekoek Institute for Astronomy, University of Amsterdam, 1090 GE Amsterdam, The Netherlands*
[10] *Center for Astrophysics, Harvard & Smithsonian, 60 Garden Street, Cambridge, MA 02138, USA*

Accepted XXX. Received YYY; in original form ZZZ

ABSTRACT

Double white dwarf binary star systems have long been considered to be a major contributor to the observed rates of type Ia supernovae, yet no observed super-Chandrasekhar mass double white dwarf binary is known that will merge in close to a Hubble time. Through a large search of candidate high-total-mass systems in the double-lined double white dwarf (DBL) survey, the source WDJ181058.67+311940.94 was found to have an atmospherically-derived total mass that exceeds $1.4\,M_\odot$. We present a follow-up campaign that reveals an orbital period of 14.24 hr and individual star masses of $0.834 \pm 0.039\,M_\odot$ and $0.721 \pm 0.020\,M_\odot$. The system therefore has a super-Chandrasekhar total mass of $1.555 \pm 0.044\,M_\odot$, making it the largest total mass double white dwarf found to date. We predict that the binary system will explode dynamically via a double detonation destroying both white dwarfs just before they merge. It will look like a subluminous type Ia supernova with a peak apparent magnitude of about $m_V = -16$ and this event will occur in 22.6 ± 1.0 Gyr. The nearby vicinity of WDJ181058.67+311940.94 at 49 pc indicates an observationally-derived birthrate of super-Chandrasekhar mass double white dwarfs of at least $6.0 \times 10^{-4}\,\mathrm{yr}^{-1}$ and a rate of type Ia supernovae from such systems of approximately $1.9 \times 10^{-4}\,\mathrm{yr}^{-1}$, while the type Ia supernova rate in the Milky Way from all progenitor channels is predicted to be about ten times larger. Hence, the discovery of WDJ181058.67+311940.94 mitigates the observed deficit of massive double white dwarfs witnessed in volume-complete populations, but further evidence is required to prove double degenerates as the majority progenitors of type Ia supernovae.

Key words: stars: close binaries: – stars: white dwarfs – supernovae: general

1 INTRODUCTION

Binaries comprising at least one white dwarf (WD) are the progenitors of type Ia supernovae (Iben & Tutukov 1984; Nugent et al. 2011; Bloom et al. 2012). Type Ia supernovae show an absence of hydrogen in their spectrum and are caused by the thermonuclear explosion of a carbon-oxygen WD. Nuclear fusion transforms a significant amount of, or the entire WD, into heavier elements and ejects them into the interstellar medium. However, the stellar type of the companion to the WD in type Ia progenitors remains largely unclear (e.g. Howell 2011; Maoz & Mannucci 2012; Liu et al. 2023; Soker 2024).

In compact binary evolution, two stars form from the same gas and dust with the same metallicity. Around 25% of binaries interact (Willems & Kolb 2004) and the evolution of at least one of the two stars is often sped up through phases of mass transfer (Postnov & Yungelson 2014), leading to a premature shedding of the outer envelope, be it by stably transferring mass or through a common envelope event (Livio & Soker 1988). Ultimately, one potential evolutionary channel forms a double WD (DWD) binary on a compact orbit with an orbital period on the timescale of hours to days (Nelemans et al. 2001) which gradually loses orbital angular momentum through gravitational wave radiation, drawing the two stars closer (Thorne 1980). Their substantial population size (Marsh 2011) has led to DWDs being one of the leading progenitor candidates to explain the abundance of type Ia supernovae (Webbink 1984; Iben & Tutukov 1984), and the larger the total system mass, the higher the rate of angular momentum loss from the system. This indicates that DWD binaries with total masses between 1.0–1.5 $M_\odot$ require a cur-

★ Email: james.munday98@gmail.com

Table 1. Positional, atmospheric and orbital parameters for WDJ181058.67+311940.94. The primary and secondary stars correspond to the more massive and less massive components, respectively. The temperatures, surface gravities and masses quoted are the adopted values from the spectroscopic fits, which were determined considering data from all sources (see Table 2).

Parameter	Unit	Value	Uncertainty
Right ascension, α	deg (2016)	272.744360834	±0.000000005
Declination, δ	deg (2016)	31.327961071	±0.000000005
Reference epoch, T_0	HJD (UTC)	2458587.6643	±0.0015
Orbital period, P	day	0.5931487	±0.0000008
Gaia parallax, π_G	mas	20.438	±0.023
Fitted parallax, π	mas	20.402	±0.003
Primary temperature, T_1	K	17 260	+1380/−880
Secondary temperature, T_2	K	20 000	+400/−2000
Primary surface gravity, $\log(g_1)$	dex	8.350	+0.066/−0.052
Secondary surface gravity, $\log(g_2)$	dex	8.164	+0.027/−0.030
Primary mass, M_1	$M_\odot$	0.834	±0.039
Secondary mass, M_2	$M_\odot$	0.721	±0.020
System mass, M_T	$M_\odot$	1.555	±0.044
Primary semi-amplitude, K_1	km s^{-1}	93.9	±2.0
Secondary semi-amplitude, K_2	km s^{-1}	95.7	±2.1
Primary velocity offset, γ_1	km s^{-1}	50.0	±1.5
Secondary velocity offset, γ_2	km s^{-1}	53.5	±1.6
Merger time, T_c	Gyr	22.6	±1.0

rent orbital period less than 9–12 hr to come into contact within a Hubble time.

Many compact DWDs have been discovered on the brink of coalescence (e.g. Burdge et al. 2020; Brown et al. 2020; Ren et al. 2023) and are high-amplitude gravitational wave radiators that will be detectable by space-based gravitational wave detectors in the mHz regime (Korol et al. 2017; Lamberts et al. 2019; Korol et al. 2022; Li et al. 2023; Kupfer et al. 2024). However, the typical total mass of these systems is heavily biased to be low in electromagnetic observations. An extrapolation of the observed sample to the mass distribution of the full population is hence challenging, yet crucial to unravel other poorly-understood evolutionary stages such as the common envelope phase (Nelemans et al. 2000, 2001; van der Sluys et al. 2006; Woods et al. 2012; Toonen et al. 2012; Ivanova et al. 2013) and stable mass transfer (Temmink et al. 2023; Li et al. 2023).

In current synthetic models of the population, DWDs with total mass greater than the Chandrasekhar mass limit are indeed suspected to be scarce (Toonen et al. 2012; Rebassa-Mansergas et al. 2019; Li et al. 2023), but based on the models of Toonen et al. (2012) we still expect about 6 compact double white dwarf binaries to have total masses that exceed 1.5 $M_\odot$ within 100 pc. However, we have had no direct evidence that these systems exist in volume-complete populations (Toonen et al. 2017; Hollands et al. 2018; O'Brien et al. 2024), casting doubt on whether DWDs can account for a large percentage of the observed type Ia supernova rates (Maoz & Mannucci 2012). There has been only one super-Chandrasekhar mass DWD binary discovered (NLTT 12758, Kawka et al. 2017), but its 1.15 d period means that the two stars will come into contact in about 10 Hubble times. There are a handful of other high-mass, candidate subluminous type Ia progenitors that are DWDs (e.g. Maxted et al. 2002; Karl et al. 2003; Nelemans et al. 2005; Rebassa-Mansergas et al. 2017; Munday et al. 2023, 2024), two WD+hot subdwarf systems that exceed 1.4 $M_\odot$ and have an impending supernova fate (Pelisoli et al. 2021; Luo et al. 2024) and one other WD+hot subdwarf that is also strong candidate (Maxted et al. 2000; Geier et al. 2007).

Type Ia supernovae initiated from the WD+hot subdwarf channel are observationally expected at a rate of at least $(1.5–7) \times 10^{-5}$ yr^{-1} (Pelisoli et al. 2021), while the rate of type Ia supernovae in the Galaxy from all progenitors is about $2.8 \pm 0.6 \times 10^{-3}$ yr^{-1} (Li et al. 2011; Maoz et al. 2014; Li et al. 2023; Liu et al. 2023), inferred through observations of explosions in other galaxies of similar redshift. Multiple other evolutionary scenarios have been suggested as causes for normal and peculiar type Ia supernovae (see Liu et al. 2023) having different companion compositions, but the extent to which they contribute towards the missing fraction of type Ia supernovae is unclear. This ambiguity on the nature of type Ia progenitors is cosmologically problematic. A primary reason is that, until we confirm the leading progenitors of a type Ia, systematic errors to the distances derived to other galaxies could lead to inaccurate measurements, which is particularly troublesome for galaxies at high redshifts (Pan et al. 2012; Maoz et al. 2014). In addition, the details of the ejecta velocity and its constituents are important for star formation (Lacchin et al. 2021) and the dynamics of gas in galaxies (Jiménez et al. 2015). Massive DWDs are one of the most attractive channels for SNe Ia and, if the progenitor age is the predominant effect controlling SN luminosity, the WDs in a young galaxy will be massive ones as these have evolved more quickly. This hypothesis can be directly tested with massive DWDs in the Milky Way. Not only would the discovery of local, compact, super-Chandrasekhar mass DWDs have the ability to resolve the dearth of systems in the observed sample, but a sample of such systems has the power to reduce uncertainty of this cosmologically fundamental event.

In this study, we present the first super-Chandrasekhar mass DWD to have a compact orbit (P = 14.24 hr) which will likely explode as a subluminous type Ia supernova in 22.6±1.0 Gyr. The individual mass constituents are 0.834 ± 0.039 $M_\odot$ and 0.721 ± 0.020 $M_\odot$, making it the most massive DWD binary discovered to date, while being located on our Galactic doorstep at 49 pc. Our observations taken as part of a follow-up campaign are outlined in Section 2, our methods and results of spectral fitting are found in Section 3 and Section 4, while we perform modelling of the final state of the system in Section 5.

2 OBSERVATIONS

WDJ181058.67+311940.94 was first discovered as part of the DBL survey (Munday et al. 2024) using medium-resolution spectra (R = 8 800) on the 4.2 m William Herschel Telescope with the

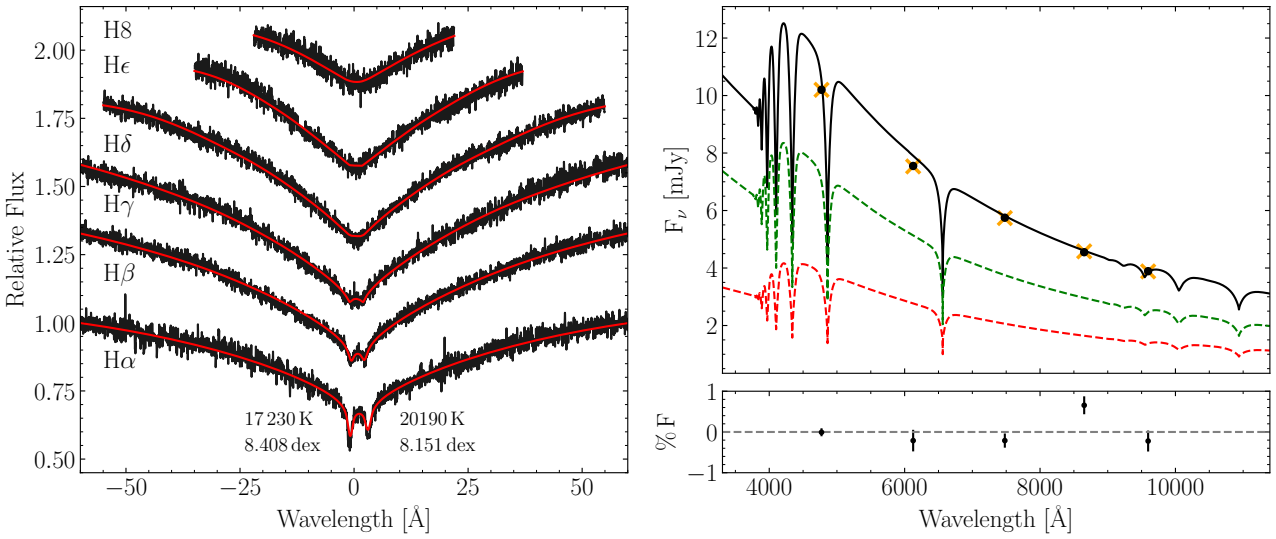

Figure 1. The results of a hybrid fit to the UVES spectra and the Pan-STARRS photometry. Left: A single UVES spectrum from Hα to H8 with the synthetic spectral model for atmospheric parameters $T_{\rm eff,1}$ = 17 230 K, $\log(g_1)$ = 8.408 dex, $T_{\rm eff,2}$ = 20 190 K, $\log(g_2)$ = 8.151 dex, overplotted in red. We remind that all Balmer lines up to H11 were fit but are omitted from the plot for clarity, and that all spectra with a split double-lined feature were fit simultaneously. Right: The observed fluxes in Pan-STARRS (black circles) and the synthetic photometry in each filter for the same atmospheric parameters (orange crosses). The percentage flux residual between the data and the combined flux is found below. The flux contributed from the more massive (dashed red) and less massive (dashed green) stars are included underneath.

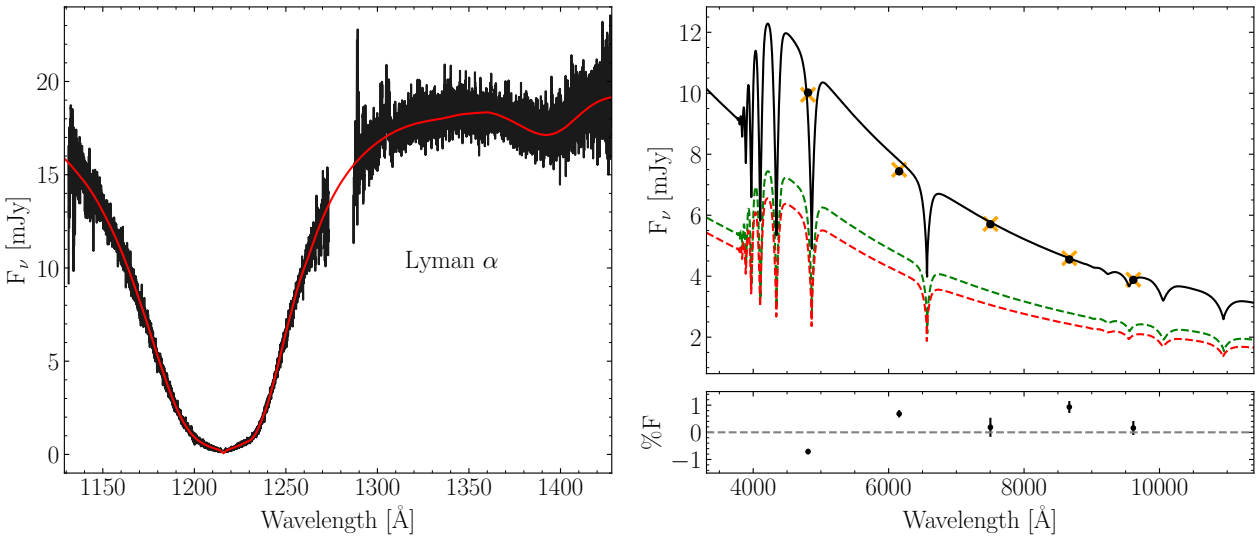

Figure 2. The results of a hybrid fit to the HST/COS ultra-violet spectrum with Pan-STARRS photometry for a two-star model. The synthetic spectra of DA WDs with atmospheric parameters $T_{\rm eff,1}$ = 18 630 K, $\log(g_1)$ = 8.307 dex, $T_{\rm eff,2}$ = 18 010 K, $\log(g_2)$ = 8.178 dex, are included. See Fig. 1 for further details.

Table 2. The atmospheric parameters for each spectroscopic data set. Hybrid fitting was performed in all cases using Pan-STARRS photometry. A systematic difference between the ultra-violet spectroscopy and the optical photometry was considered in the fitting (Section 3.2). Masses are inferred by interpolation of the evolutionary sequences in Bédard et al. (2020) and M_T is the total mass of the system. The final adopted values were obtained by concatenating the distributions obtained for each parameter to then quote the median and 68% confidence interval on the $T_{\rm eff}$ and $\log(g)$, while interpolating to find masses. The more/less massive star is labelled with subscript 1/2 respectively. The WHT/ISIS solution is quoted from the result of Munday et al. (2024).

Telescope / Instrument	$T_{\rm eff,1}$ [K]	$\log(g_1)$ [dex]	M_1 [$M_\odot$]	$T_{\rm eff,2}$ [K]	$\log(g_2)$ [dex]	M_2 [$M_\odot$]	M_T [$M_\odot$]
VLT/UVES	17230 ± 710	8.408 ± 0.027	0.871 ± 0.018	20190 ± 280	8.151 ± 0.021	0.713 ± 0.014	1.584 ± 0.022
WHT/ISIS	16500^{+400}_{-300}	8.35 ± 0.05	0.83 ± 0.03	20200 ± 300	8.16 ± 0.04	0.72 ± 0.03	1.55 ± 0.04
HST/COS	18630 ± 80	8.307 ± 0.020	0.810 ± 0.013	18010 ± 70	8.178 ± 0.018	0.727 ± 0.013	1.537 ± 0.018
Adopted	17260^{+1380}_{-880}	$8.350^{+0.066}_{-0.052}$	0.834 ± 0.039	20000^{+400}_{-2000}	$8.164^{+0.027}_{-0.030}$	0.721 ± 0.020	1.555 ± 0.044

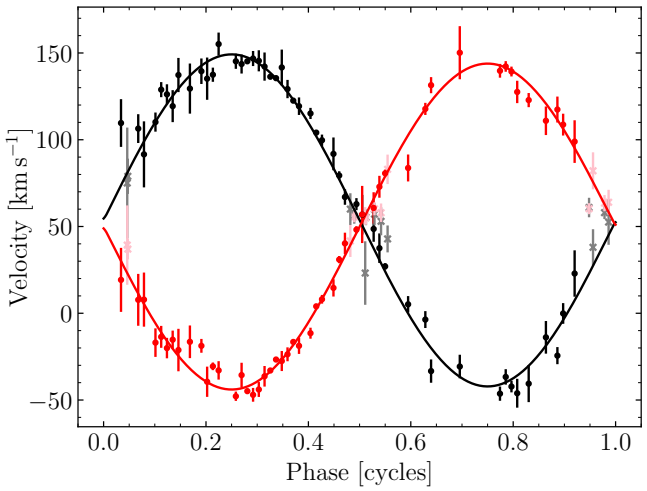

Figure 3. Left: The best-fit orbital solution phase-folded on the orbital period. In black points, the hotter star, and in red the cooler star. The RV curves are plotted showing the velocity of the two stars across a full orbit, binned into 80 evenly spaced phase bins. In faded colours and with crossed markers are the RVs that were masked in searching for an orbital solution (see Section 3.3 for details).

Intermediate-dispersion Spectrograph and Imaging System (ISIS). Two other ISIS exposures were taken on the nights 13 & 14 April 2019 using the R600B and R1200R gratings with 1.2″slit resulting in a resolution of R = 3 000 at Hα and these spectra are included in the full orbital analysis of the DWD. The blue and red setups had a wavelength calibration accuracy of approximately 3 km s^{-1} and 2 km s^{-1}, respectively.

We conducted a continued observational campaign to derive phase-resolved radial velocities (RVs) of the DWD binary. We utilised the 2.5 m Isaac Newton Telescope (INT) with the Intermediate Dispersion Spectrograph (IDS) over the nights 4-7 September 2019 (11 exposures, 1800 s each), and 24 September 2019 (4 exposures, 900 s each) with the Red+2 detector and a 1.2″slit width, resulting in a spectral resolution of R = 6 300. Further phase-resolved spectra were taken with the INT telescope on the nights 25 & 26 August 2024 with the H1800V grating at a resolution of R = 9 400 (20 exposures, 1500 s each). An arc lamp exposure was taken every 45 min of observing time and the science images were wavelength calibrated by interpolation of the nearest two arcs. The wavelength calibration accuracy per frame was approximately 2 km s^{-1}.

Bias, flat field and spectrophotometric flux standard star images were taken on all nights and applied in the reduction. All data from the WHT and the INT were reduced using the MOLLY suite (Marsh 2019), with the optimal extraction algorithm outlined in Marsh (1989).

We supplemented data from the INT and WHT with continued spectroscopic observations through 18 exposures of length 1 500 s on the 2.56 m Nordic Optical Telescope (NOT) using the FIbre-fed Echelle Spectrograph (FIES) in low-resolution mode. These granted full optical coverage at a resolution R = 25 000 with a wavelength calibration accuracy of approximately ±150 m s^{-1}. Observations were obtained through a staff queue at random times, typically being two consecutive exposures, and through a NOT fast-track proposal. All FIES data were reduced using its automated data reduction pipeline – FIEStool[1]. We also obtained 5 exposures with the NOT Alhambra Faint Object Spectrograph and Camera (ALFOSC) with a 0.5″slit width, producing spectra at R=10 000 with wavelength range 6330-6870 Å. These were taken on 1 & 2 June 2024, and the data were reduced with the PYPEIT python package (Prochaska et al. 2020).

A continuous observing window of 4.5 hr was obtained through directors discretionary time on the 8.2 m Very Large Telescope (VLT) with the UV-Visual Echelle Spectrograph (UVES). Each exposure lasted for 730 s with a readout time between exposures of 45 s, totalling 20 exposures. We employed an observing setup of the dichroic 1 mode with central wavelengths of 3900 Å and 5640 Å for the blue and red arm, giving a wavelength range that covered the full visible spectrum besides gaps of 80 Å at 4580 Å and 5640 Å. A slit width of 1.0” and a 2×2 binning granted a spectral resolution R = 20 000 and the wavelength calibration accuracy was approximately 200 m s^{-1} (Whitmore et al. 2010; Whitmore & Murphy 2015).

In deriving final RVs for these data (Table A1), the wavelength calibration error was added in quadrature to the statistical error.

3 SPECTRAL ANALYSIS

3.1 Atmospheric fitting of optical data

We used the package WD-BASS[2] (Munday 2024) to fit atmospheric parameters to the spectra from VLT/UVES. For synthetic spectra, we utilised the 3D-NLTE model grid introduced in Munday et al. (2024), which was constructed using the 3D-LTE models of Tremblay et al. (2015) with a further NLTE correction factor applied using the NLTE and LTE synthetic spectra described in Kilic et al. (2021). The two stars were scaled using temperature-log g-radius relationships with the evolutionary track models of Istrate et al. (2016) when M ≤ 0.393 M$_\odot$, Althaus et al. (2013) when 0.393 < M < 0.45 M$_\odot$ and the hydrogen-rich evolutionary sequences of Bédard et al. (2020) otherwise. The model spectra were converted from an Eddington flux to that observed at Earth and reddened with A(V) = 0.0312 mag (Lallement et al. 2022), E(B-V) = A(V)/3.1 using the reddening curves of Gordon et al. (2023).

We applied an atmospheric fitting technique that is very similar to that described in Munday et al. (2024), performing a hybrid fit with the UVES spectra and Pan-STARRS photometry (Chambers & Pan-STARRS Team 2018) simultaneously. The differences were that, because of the improved signal-to-noise ratio of the data, we could fit bluer Balmer lines being all from Hα to H11. Then secondly, to give the photometric and spectroscopic data a similar overall weight, we applied an extra weighting (×1000) to the photometric fit. Without this weighting, the spectra would have over-dominated the best-fit solution. Only spectra taken at the times where a distinct double-line splitting is evident at Hα were fit to avoid fitting degeneracies between the two stars, which were 10 of them (total of 20). In deriving errors, we individually fit each red-arm spectrum that reveals a double-lined Hα split along with the nearest-in-time blue-arm spectrum while weighting the photometry by 100×. Then, we took the standard deviation of all measurements to be the error in star’s surface gravity and temperature. The new best-fit atmospheric parameters are stated in Table 2, which are entirely consistent with those found in Munday et al. (2024).

3.2 Atmospheric fitting of ultra-violet data

We performed an independent spectroscopic fit using the Hubble Space Telescope spectrum presented in Sahu et al. (2023).

[1] https://not.iac.es/instruments/fies/fiestool/FIEStool.html

[2] https://github.com/JamesMunday98/WD-BASS

WDJ181058.67+311940.94 was observed for a single 1 000 s exposure using the Cosmic Origins Spectrograph on the 19th February 2022 with the centre of exposure at 05:00 UT. The observation had a central wavelength of 1291 Å with the G130M grating, giving a resolution of R = 12 000–16 000 and a wavelength range of 1130–1430 Å with a gap at 1278–1288 Å due to the positioning of the two detector segments. Given the vastly different method and the fact that WDJ181058.67+311940.94 is not double-lined at Lyman-α in the ultra-violet data, no RVs were extracted, but the predicted RVs of the two stars at the centre of exposure ($-37.8\,\mathrm{km\,s^{-1}}$ for the more massive and $139.6\,\mathrm{km\,s^{-1}}$ for the less massive star, respectively) were fixed in the fitting procedure.

Our spectral fitting method is identical to that presented in Sahu et al. (2023) with the only exceptions being that a second hydrogen-rich atmosphere WD is included in the model, that we adopt A(V)=0.0312 mag and that the mid-exposure RV of the two stars is considered. A hybrid (spectroscopic and photometric) fit was performed with no extra error weighting applied, using the HST/COS spectrum and photometry from Pan-STARRS g, r, i, z, y (Chambers & Pan-STARRS Team 2018), fixing the distance to *Gaia* DR3 parallax. Updated model atmospheres from Koester (2010) with a WD mass-radius relation extracted from Bédard et al. (2020) were used to fit the absolute fluxes. Additionally, strong absorption lines affecting the continuum were masked in the COS spectrum (Sahu et al. 2023). To address the inconsistencies reported between ultra-violet and optical parameters (Sahu et al. 2023), a systematic offset of 1% in $T_{\rm eff}$ and 0.1 dex in log(g) were added to the ultra-violet values of both stars in the hybrid fitting, while trial values in the optical were unchanged. The best-fit model to the spectra are shown in Fig. 2, and the results of our atmospheric fitting in Table 2 with comparison to the optical solution. We found a total mass of $1.537 \pm 0.018\,\mathrm{M_\odot}$ through this analysis, which again is consistent with that stated in Munday et al. (2024).

To provide a final adopted value from the atmospheric fitting inclusive of the results from the optical and the ultra-violet datasets, we concatenated the distributions obtained for each parameter to then quote the median and 68% confidence interval on the $T_{\rm eff}$ and $\log(g)$, while interpolating these parameters to find obtain masses. The adopted values are quoted in Tables 1 and Table 2.

3.3 Radial velocities and orbital parameters

WD-BASS was again used to obtain radial velocities (RVs) for all of the optical spectra. The best-fit synthetic spectrum agrees with the data extremely well (see Fig. 1), but even with the correction of NLTE effects to the model grid line cores, the synthetic model flux is over-predicted in the line cores of Hα. To obtain the most accurate template for RV extraction possible, we fit a Gaussian model to the Hα line cores of both stars combined with a 4-term polynomial to model the broader wings of Hα, all within 10 Å of the Hα centre. This method best modelled the shape of the spectral area around the line cores for the high signal-to-noise ratio and high resolution UVES spectra, but not for all other data sources. Instead, we took the result of the best-fit synthetic spectrum and added an extra Gaussian component at the line cores of Hα for both stars (following the method described in Section 4.4 of Munday et al. 2024), which improved the line-core shape significantly. The Gaussians were fit to all relevant spectra simultaneously and this final template spectrum was then used for RV extraction in WD-BASS. We started by fitting the RV of both stars to each spectrum by taking the median of 1000 bootstrapping iterations and taking errors as the standard deviation of this bootstrapped posterior distribution.

With the full set of 82 RV measurements (Appendix A), we then searched for an orbital period, P, by minimising the χ^2 of equation 1 for trial semi-amplitudes (K_1, K_2) and velocity offsets (γ_1, γ_2) of each star using a least squares algorithm, where

$$\mathrm{PK}^3_{1,2} = \frac{2\pi \mathrm{GM}^3_{2,1}\,\sin(i)^3}{(\mathrm{M}_{1,2}+\mathrm{M}_{2,1})^2} \quad (1)$$

An upper bound on the semi-amplitude, $K_{\rm max,1}$ and $K_{\rm max,2}$ were set for a trial period set by applying an edge-on ($i = 90°$) inclination for a $1.4\,\mathrm{M_\odot} + 0.15\,\mathrm{M_\odot}$ DWD in a Keplerian orbit (the maximum and observed minimum mass of a WD, respectively). There is no indication of eccentricity from the RVs, so the orbit is assumed to be circularised ($e = 0$).

In the process, we noticed a deviation from Keplerian motion around conjunction which is caused by degeneracy in the fitted RVs as the stars spectrally overlap. This is unsurprising as the velocity resolution of the ALFOSC, ISIS and IDS data was around 30–40 $\mathrm{km\,s^{-1}}$, while in the higher resolution FIES spectra a lower signal-to-noise ratio of the spectra led to the same degeneracies. We decided to ignore these RVs when fitting the orbital motion by masking measurements which are within $15\,\mathrm{km\,s^{-1}}$ of the RV of each star at conjunction. All RVs from the UVES spectra within this range were utilised as its high signal-to-noise combined with twice the velocity resolution did not cause any noticeable deviation.

Our phase-folded RV curve with the best-fit orbital solution is depicted in Fig. 3. The best-fitting orbital parameters are $P = 14.23557 \pm 0.00002$ hr, $K_1 = 93.9 \pm 2.0\,\mathrm{km\,s^{-1}}$, $K_2 = 95.7 \pm 2.1\,\mathrm{km\,s^{-1}}$, $\gamma_1 = 50.0 \pm 1.5\,\mathrm{km\,s^{-1}}$, $\gamma_2 = 53.5 \pm 1.6\,\mathrm{km\,s^{-1}}$. Being double-lined, the mass ratio is independently solvable without knowledge of the orbital inclination with $q = \mathrm{M_2/M_1} = \mathrm{K_1/K_2}$, such that the orbitally derived $q = 0.98 \pm 0.03$. This result is in best agreement with the star masses derived from the HST/COS spectrum, which was $q = 0.90 \pm 0.02$. Our derived masses from the VLT/UVES spectra yield a lower $q = 0.82 \pm 0.02$, with the mass of the less massive star being near identical to the ultra-violet, and the adopted value taking into account all measurements indicates a mass ratio of $q = 0.86 \pm 0.04$. The surface gravity of the hotter, less massive star is near identical across fits to all datasets. This is unsurprising given that it contributes more flux than the dimmer WD, while its temperature difference between the ultra-violet and optical datasets primarily arises from the fitting of the slope of the spectral energy distribution across the ultra-violet. Forcing the orbitally-derived $q = 0.98 \pm 0.03$ in the atmospheric fit requires the surface gravity of the secondary to increase and the surface gravity of the primary to decrease to fit the broadness of the Balmer line profiles well. The secondary would thus be more massive, the primary less massive and as such, including for a mass ratio of approximately one, the binary is a super-Chandrasekhar mass DWD.

All evidence strongly points towards the total mass of WDJ181058.67+311940.94 being significantly above the Chandrasekhar mass limit and that the two have similar masses. Galactic population models predict that about half of super-Chandrasekhar mass systems contain similar mass stars within $0.2\,\mathrm{M_\odot}$ of each other (Toonen et al. 2012), as is the case also for NLTT 12758, where all systems with $q \gtrapprox 2/3$ are destined to undergo unstable mass transfer (Marsh et al. 2004). Unstable mass transfer will hence occur in the future for WDJ181058.67+311940.94 as well.

Returning to equation 1 with mass constraints, we can solve for the orbital inclination, i. By taking into account all combinations of masses determined from the atmospheric analysis, we conclude that WDJ181058.67+311940.94 has an inclination $i \approx 35-45$ deg. We analysed the TESS (Ricker et al. 2015) light curve of

WDJ181058.67+311940.94 in all cadences to search for any photometric signature of photometric variability with Lomb-Scargle (Lomb 1976; Scargle 1982) and boxed-least-squares periodograms but found no variation on the orbital period. For an eclipse to be witnessed in this system, the inclination would have to be above 89.64 deg and photometric variability from ellipsoidal modulation or irradiation is minute for a system with 14.24 hr orbital period. The Doppler beaming effect of the two stars is nullified by their opposing motion of near-identical RV amplitudes and a similar flux contribution (Hermes et al. 2014), hence non-eclipsing forms of variability are not expected.

4 MERGER TIME AND POPULATION RATE

The critical time at which the merger will occur is calculable using (Peters 1964)

$$T_c(a_0) = \frac{5}{256}\frac{a_0^4 c^5}{G^3 M_1 M_2 (M_1 + M_2)} \quad (2)$$

where a_0 is the semi-major axis of the binary at present day and, for WDJ181058.67+311940.94, $a_0 = 0.01601 \pm 0.00015$ AU. This indicates that the type Ia supernova will occur in 22.6 ± 1.0 Gyr, while the less-massive component will begin Roche lobe overflow and initiate mass transfer approximately 100 yrs before the demise of binary.

We can use WDJ181058.67+311940.94 to observationally predict the number of super-Chandrasekhar mass DWDs in the Milky Way. If we assume that WDJ181058.67+311940.94 and NLTT 12758 are the only two within 49 pc and make the rudimentary assumption that DWDs are evenly scattered around the Milky Way, a cylindrical disk with radius $R_{max} = 15$ kpc and scale height $h_z = 300$ pc indicates approximately 861 000 systems in the Galaxy. Holberg et al. (2016) estimate a present WD birth rate of $\approx 1.4 \times 10^{-12}$ pc^{-3} yr^{-1}, there are 1076 WDs within the volume complete 40 pc sample (O'Brien et al. 2024) and extrapolated to 49 pc we would have 1978 WDs. This means that the birth rate of super-Chandrasekhar mass DWDs in the Galaxy becomes greater than approximately 6.0×10^{-4} yr^{-1}.

Moreover, we can also calculate an observed rate of type Ia supernovae arising from super-Chandrasekhar mass double white dwarfs using WDJ181058.67+311940.94 ($T_c = 22.6 \pm 1.0$ Gyr) and NLTT 12758 ($T_c = 139 \pm 9$ Gyr). The frequency of the two events combined imply a supernova rate of about once every 19 Gyr within 49 pc, or $(4.37 \pm 0.17) \times 10^{-16}$ yr^{-1} pc^{-3}. When fully extrapolated with the cylindrical disk approximation, the observed rate of type Ia supernovae from super-Chandrasekhar mass double white dwarfs in the Milky Way hence becomes at least $(1.85 \pm 0.07) \times 10^{-4}$ yr^{-1}, though the quoted uncertainty does not account for uncertainties on the Galactic model. This result serves as a minimum based on the 49 pc population as it remains possible that other systems exists within the same radius.

Evidently, the magnitude of super-Chandrasekhar mass systems approaches the $(2.8 \pm 0.6) \times 10^{-3}$ yr^{-1} rate predicted for all evolutionary channels leading to a type Ia (Li et al. 2011; Maoz et al. 2014; Liu et al. 2023), but we must recall that these two systems are set to come together in over a Hubble time and consider that the present observed supernova rate from these systems is about ten times smaller. Contribution to the double white dwarf type Ia rate from sub-Chandrasekhar mass limits detonation could at least be a partial solution to make up for the deficit, where a mass-period distribution of DWDs in a volume/magnitude limited sample serves as a means to put this to the test (Munday et al. 2024). Ongoing efforts are crucial to properly quantify the number of massive DWD binaries in our local neighbourhood and the Milky Way, while deeper, volume-complete spectroscopic samples of WDs in all locations of the Hertzsprung-Russell diagram will become possible in the next decades through multi-object spectrograph surveys.

5 MODELLING THE FATE OF THE BINARY SYSTEM

To understand the fate of the binary system we simulate its interaction when it is just about to merge. We use the moving-mesh code AREPO (Springel 2010; Pakmor et al. 2016; Weinberger et al. 2020) in a similar setup as in Pakmor et al. (2022); Glanz et al. (2024). Here we summarise the setup and simulation with an emphasis on improvements compared to Pakmor et al. (2022). A detailed description and analysis will be presented as part of a large parameter study of WDs mergers in the near future, of which the simulation shown here is the forerunner.

We first created two white dwarfs from the pre-main sequence phase using the stellar evolution code MESA (Paxton et al. 2011, 2013, 2015, 2018, 2019; Jermyn et al. 2023), evolving them to carbon-oxygen white dwarfs of 0.87 $M_\odot$ and 0.71 $M_\odot$. These masses align with observations from VLT/UVES spectra fitting. Compared to previous merger simulations, using self-consistent models evolved in MESA allows us to start from realistic composition profiles. In particular, the two WDs have a helium shell of 8×10^{-3} $M_\odot$ (for the 0.71 $M_\odot$ WD) and 3×10^{-3} $M_\odot$ (for the 0.87 $M_\odot$ WD), respectively.

We then created two 3D WDs in hydrostatic equilibrium with the same masses and abundance profiles in AREPO. We resolved the WDs with cells with a roughly constant mass of 10^{-7} $M_\odot$ and used a passive scalar to resolve the helium shells of both WDs even better with a mass resolution of 10^{-8} $M_\odot$. We relaxed both WDs in isolation for 10 dynamical timescales, actively dampening any gas velocities for the first half of this time. The density and composition profiles of the relaxed WDs, in particular close to the surface, well resemble the initial 1D profiles obtained from MESA.

We put both WDs into a binary system in co-rotation with an initial period of 73 s. At this period the separation is about 1.5 times larger than the separation where the secondary WD will fill its Roche-lobe. We apply an accelerated inspiral term that removes angular momentum in the same way as gravitational waves, but on a much faster timescale. This way we obtain a binary system in equilibrium when mass transfer starts on a scale that we can resolve in the simulation. At this time, the physical system will have transferred mass at a low rate for possibly thousands of years, but the total mass transferred is likely negligible. The secondary WD eventually starts filling and then overfilling its Roche-lobe, and we stop the accelerated inspiral when the density at the inner Lagrange point between the WDs reaches 2×10^4 g cm^{-3}. Only then the density in the accretion stream becomes large enough to dynamically affect the surface of the primary WD (Guillochon et al. 2010; Pakmor et al. 2013, 2022).

The binary system has now shrunk to a separation of 0.03 $R_\odot$ and an orbital period of 39 s. We then continue to evolve the binary system conservatively and switch on a live nuclear reaction network with 55 isotopes (Pakmor et al. 2012, 2022). We show an overview of the dynamic evolution of the binary system in Fig. 4. After evolving the binary system conservatively for 55 s the interaction of the accretion stream with the surface of the primary WD ignites a helium detonation close to the point of interaction (second column of Fig. 4), consistent with previous simulations of more massive WD binaries (Pakmor et al. 2013, 2021, 2024). As in the classic double detonation scenario where the helium detonation is caused by instabilities

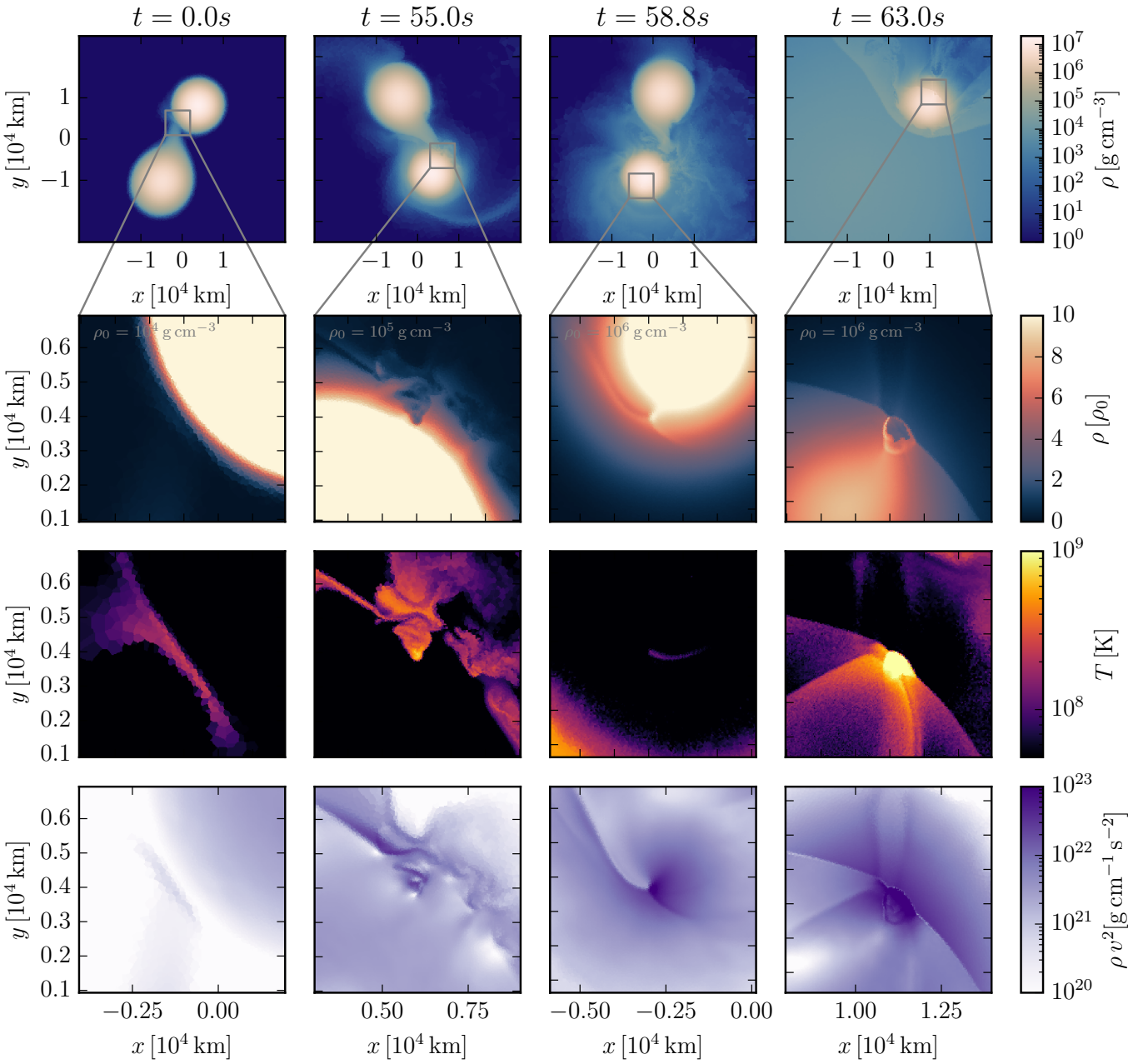

Figure 4. Time evolution in slices of the binary systems close to merger. The first column shows the time when we stop the accelerated inspiral and continue to evolve the binary system self-consistently. The second and third columns show the time when the helium detonation ignites on the surface of the primary WD, and the time when the shock wave that is driven into the core of the primary by the helium detonation converges in a single point. The fourth column shows the same shock convergence in the core of the secondary WD. The top row shows slices of density in the plane of rotation and the three below are zoomed insets at the point of interest. From top to bottom: density, temperature, and kinetic energy density. The qualitative evolution is very similar to the more massive binary system discussed in Pakmor et al. (2022). The shock convergence points in both WDs occur at densities high enough to very likely ignite a carbon detonation and destroy the WD.

in a massive helium shell (Livne 1990; Fink et al. 2010), the helium detonation wraps around the primary WD. It sends a shock wave into the core of the WD, that converges in a single point at a density of $9.6 \times 10^6\,\mathrm{g\,cm^{-3}}$. Because of a lack of numerical resolution, the simulation does not self-consistently ignite a carbon detonation there, but resolved ignition simulations indicate that at this density we expect a detonation to form at the convergence point (Seitenzahl et al. 2009; Shen & Bildsten 2014). To model the ignition of the detonation when the shock converges in the simulation, we set the temperature of 178 cells that contain $1.8 \times 10^{-5}\,M_\odot$ around the convergence point to 5×10^9 K. This injects 4.8×10^{46} erg (negligible compared to the energy release of the whole simulation) and ignites the detonation. The detonation completely destroys the primary WD. When the shock wave of its explosion hits the secondary WD, the

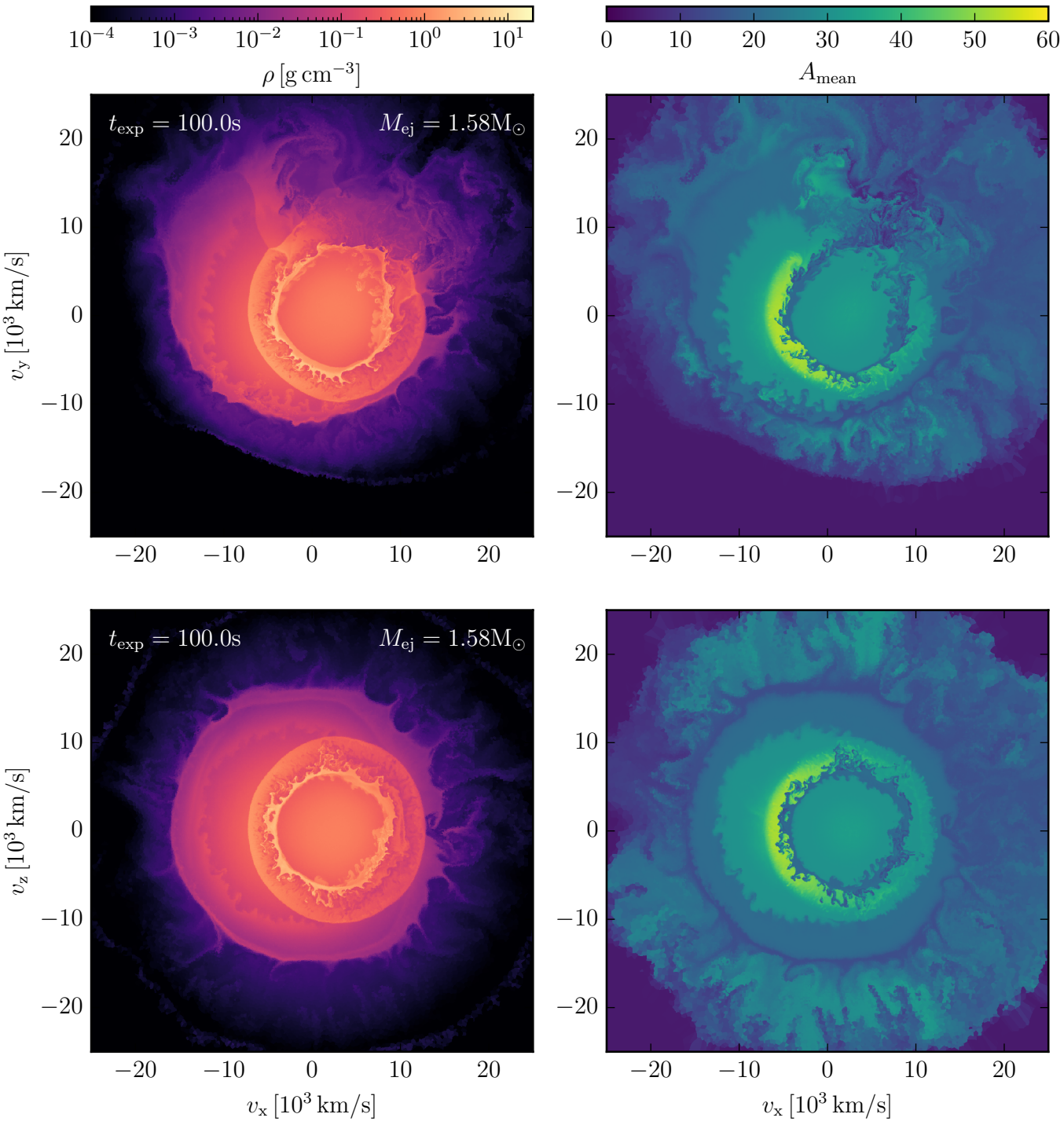

Figure 5. Slices of density (left column) and mean atomic weight (right column) of the supernova ejecta in homologous expansion 100 s after ignition of the first helium detonation. The top row shows slices in the original plane of rotation, the bottom row slices perpendicular to it. The outer layers are close to spherically symmetric, though significant deviations from spherical symmetry exist in the plane of rotation. The iron group elements (including ^{56}Ni) are essentially all produced in the explosion of the primary WD and form a half-sphere around the ejecta of the secondary WD.

double detonation mechanism repeats itself. The shock wave ignites a helium detonation that drives a shock wave into the core and converges at a density of 8.5×10^6 g cm^{-3}. In this case carbon burning even starts at the convergence point, but not strongly enough to start a detonation. We again ignite a detonation at the convergence point by setting the temperature of 708 cells that contain $6.9 \times 10^{-5}\,M_{\odot}$ to 6×10^9 K, which injects 8.2×10^{47} erg and is sufficient to ignite the detonation that then destroys the secondary WD as well.

There is no bound remnant and the ejecta of the explosion contain the full 1.58 M$_{\odot}$ of the initial binary system, having a total explosion energy of 1.2×10^{51} erg. The core of the secondary WD ignites 4.2 s after the core of the primary WD. At this time the ashes of the

primary WD have already expanded far beyond the secondary WD. So when the latter explodes as well, its ejecta expand into and remain in the centre of the ejecta of the primary WD (Pakmor et al. 2022). We show the structure and composition of the ejecta in Fig. 5. The outermost layers of ejecta are the ashes of the helium detonation of the primary WD. They consist mostly of intermediate mass elements, dominated by silicon, sulphur, and argon. Below them sit the ashes of the carbon-oxygen core of the primary WD. They again consist mostly of intermediate mass elements, but also contain $0.13\,M_\odot$ of iron group elements, in particular $0.10\,M_\odot$ of radioactive ^{56}Ni that will power the lightcurve. The centre of the ejecta consists of the ashes of the secondary WD, which contain $0.25\,M_\odot$ of oxygen, $0.4\,M_\odot$ of intermediate mass elements, and only $0.01\,M_\odot$ of iron group elements with a roughly equal fraction of ^{56}Ni and ^{54}Fe.

We obtain preliminary synthetic light curves from spherically averaging the ejecta and computing light curves with the Monte-Carlo radiation transport code ARTIS (Kromer & Sim 2009; Sim 2007). The resulting supernova has a maximum brightness in the B-band of $M_\mathrm{B} = -16.4$ ($m_B = -14.7$) and a maximum brightness in the V-band of $M_\mathrm{V} = -17.8$ ($m_V = -16.1$), consistent with traditional double detonation models of single WDs with a similar mass as our primary WD, because the secondary WD does not produce any significant amount of radioactive ^{56}Ni (Sim et al. 2010; Shen et al. 2021; Collins et al. 2022). That said, our explosion likely avoids the imprint of thick helium shells on light curves and spectra (Kromer et al. 2010; Collins et al. 2022, 2023). It will most likely appear as a sub-luminous type Ia supernova. However, the obvious large-scale asymmetries visible in Fig. 5 indicate that 3D synthetic observables will be needed to make any reliable statement about the expected display of this supernova (Collins et al. 2022; Pakmor et al. 2024). They will be presented and discussed as part of a larger sample of merger simulations in the future. This new simulation also supports previous work which suggests that both stars will explode in massive DWD binaries that are about to merge (Pakmor et al. 2022; Boos et al. 2024; Shen et al. 2024).

6 CONCLUSIONS

We have presented the first confirmed to be compact, super-Chandrasekhar mass DWD binary which will merge in close to a Hubble time (23 Gyr), having an orbital period of 14.24 hr. With a total mass of $1.555 \pm 0.044\,M_\odot$, WDJ181058.67+311940.94 is the most massive DWD binary confirmed to date, followed by one other super-Chandrasekhar mass DWD having a merger time of approximately 137 Gyr (Kawka et al. 2017). We predict it to explode as a quadruple detonation and be destroyed completely. With all the mass ejected and a total explosion energy of 1.2×10^{51} erg, but only $0.1\,M_\odot$ of ^{56}Ni in the ejecta, it will appear as a subluminous type Ia supernova with a peak apparent magnitude of approximately $m_B = -14.7$ and $m_V = -16.1$.

The lack of observational evidence of compact and massive DWD binaries has long troubled the theory that DWDs are the dominating evolutionary channel of type Ia detonations (Maoz & Mannucci 2012). WDJ181058.67+311940.94 provides tentative observational evidence that such systems with short merger times do exist in the Milky Way, and when combined with the close proximity of 49 pc the rate of super-Chandrasekhar mass DWDs born in the Milky Way is at least $6.0 \times 10^{-4}\,\mathrm{yr}^{-1}$. This draws closer the disparity between the observed and theoretical rates, though the observed is still approximately twice smaller.

Being discovered through a medium-resolution search of overluminous DWDs (Munday et al. 2024), which up to a magnitude limit of $G < 17$ is approximately 20% complete, it is entirely plausible that more super-Chandrasekhar mass DWDs reside in our Galactic neighbourhood and that we have the spectroscopic ability to resolve the formation channel of type Ia supernovae. Deeper completeness through photometric and spectroscopic surveys in the coming years, as well the inauguration of space-based gravitational wave detectors in the next decade, will be pivotal in detecting ultra-compact binaries on the cusp of detonation (Korol et al. 2017, 2024). The combined efforts surveying type Ia progenitors across the full range of orbital periods will be the ultimate means to accurately quantify the contribution of double white dwarfs to type Ia supernovae.

ACKNOWLEDGEMENTS

We thank Stephan Geier for their insightful comments during the study. JM was supported by funding from a Science and Technology Facilities Council (STFC) studentship. DJ acknowledges support from the Agencia Estatal de Investigación del Ministerio de Ciencia, Innovación y Universidades (MCIU/AEI) and the European Regional Development Fund (ERDF) with reference PID-2022-136653NA-I00 (DOI:10.13039/501100011033). DJ also acknowledges support from the Agencia Estatal de Investigación del Ministerio de Ciencia, Innovación y Universidades (MCIU/AEI) and the the European Union NextGenerationEU/PRTR with reference CNS2023-143910 (DOI:10.13039/501100011033). This research received funding from the European Research Council under the European Union's Horizon 2020 research and innovation programme number 101002408 (MOS100PC). ST acknowledges support from the Netherlands Research Council NWO (VIDI 203.061 grant). AB is a Postdoctoral Fellow of the Natural Sciences and Engineering Research Council (NSERC) of Canada. JM: coauthor acknowledgements (add as you please) Based on observations collected at the European Organisation for Astronomical Research in the Southern Hemisphere under ESO programme 113.27QU. The Isaac Newton Telescope and the William Herschel Telescope are operated on the island of La Palma by the Isaac Newton Group of Telescopes in the Spanish Observatorio del Roque de los Muchachos of the Instituto de Astrofísica de Canarias. Based on observations made with the Nordic Optical Telescope, owned in collaboration by the University of Turku and Aarhus University, and operated jointly by Aarhus University, the University of Turku and the University of Oslo, representing Denmark, Finland and Norway, the University of Iceland and Stockholm University at the Observatorio del Roque de los Muchachos, La Palma, Spain, of the Instituto de Astrofísica de Canarias. The data presented here were obtained in part with ALFOSC, which is provided by the Instituto de Astrofísica de Andalucia (IAA) under a joint agreement with the University of Copenhagen and NOT. This research is based on observations made with the NASA/ESA Hubble Space Telescope obtained from the Space Telescope Science Institute, which is operated by the Association of Universities for Research in Astronomy, Inc., under NASA contract NAS 5–26555. These observations are associated with program 16642.

DATA AVAILABILITY

All reduced data is available upon request to the authors and the relevant reduction pipelines are cited in text. Raw data is obtainable through the respective telescope data archives. The observed RVs are published in Appendix A.

References

Althaus L. G., Miller Bertolami M. M., Córsico A. H., 2013, A&A, 557, A19
Bédard A., Bergeron P., Brassard P., Fontaine G., 2020, ApJ, 901, 93
Bloom J. S., et al., 2012, ApJ, 744, L17
Boos S. J., Townsley D. M., Shen K. J., 2024, ApJ, 972, 200
Brown W. R., et al., 2020, ApJ, 889, 49
Burdge K. B., et al., 2020, ApJ, 905, 32
Chambers K., Pan-STARRS Team 2018, in American Astronomical Society Meeting Abstracts #231. p. 102.01
Collins C. E., Gronow S., Sim S. A., Röpke F. K., 2022, MNRAS, 517, 5289
Collins C. E., Sim S. A., Shingles L. J., Gronow S., Röpke F. K., Pakmor R., Seitenzahl I. R., Kromer M., 2023, MNRAS, 524, 4447
Fink M., Röpke F. K., Hillebrandt W., Seitenzahl I. R., Sim S. A., Kromer M., 2010, A&A, 514, A53
Geier S., Nesslinger S., Heber U., Przybilla N., Napiwotzki R., Kudritzki R. P., 2007, A&A, 464, 299
Glanz H., Perets H. B., Bhat A., Pakmor R., 2024, arXiv e-prints, p. arXiv:2410.17306
Gordon K. D., Clayton G. C., Decleir M., Fitzpatrick E. L., Massa D., Misselt K. A., Tollerud E. J., 2023, ApJ, 950, 86
Guillochon J., Dan M., Ramirez-Ruiz E., Rosswog S., 2010, ApJ, 709, L64
Hermes J. J., et al., 2014, ApJ, 792, 39
Holberg J. B., Oswalt T. D., Sion E. M., McCook G. P., 2016, MNRAS, 462, 2295
Hollands M. A., Tremblay P. E., Gaensicke B. T., Gentile-Fusillo N. P., Toonen S., 2018, arXiv e-prints, p. arXiv:1805.12590
Howell D. A., 2011, Nature Communications, 2, 350
Iben I. J., Tutukov A. V., 1984, ApJS, 54, 335
Istrate A. G., Marchant P., Tauris T. M., Langer N., Stancliffe R. J., Grassitelli L., 2016, A&A, 595, A35
Ivanova N., et al., 2013, A&ARv, 21, 59
Jermyn A. S., et al., 2023, ApJS, 265, 15
Jiménez N., Tissera P. B., Matteucci F., 2015, ApJ, 810, 137
Karl C. A., Napiwotzki R., Nelemans G., Christlieb N., Koester D., Heber U., Reimers D., 2003, A&A, 410, 663
Kawka A., Briggs G. P., Vennes S., Ferrario L., Paunzen E., Wickramasinghe D. T., 2017, MNRAS, 466, 1127
Kilic M., Bédard A., Bergeron P., 2021, MNRAS, 502, 4972
Koester D., 2010, Mem. Soc. Astron. Italiana, 81, 921
Korol V., Rossi E. M., Groot P. J., Nelemans G., Toonen S., Brown A. G. A., 2017, MNRAS, 470, 1894
Korol V., Hallakoun N., Toonen S., Karnesis N., 2022, MNRAS, 511, 5936
Korol V., Buscicchio R., Pakmor R., Morán-Fraile J., Moore C. J., de Mink S. E., 2024, arXiv e-prints, p. arXiv:2407.03935
Kromer M., Sim S. A., 2009, MNRAS, 398, 1809
Kromer M., Sim S. A., Fink M., Röpke F. K., Seitenzahl I. R., Hillebrandt W., 2010, ApJ, 719, 1067
Kupfer T., et al., 2024, ApJ, 963, 100
Lacchin E., Calura F., Vesperini E., 2021, MNRAS, 506, 5951
Lallement R., Vergely J. L., Babusiaux C., Cox N. L. J., 2022, A&A, 661, A147
Lamberts A., Blunt S., Littenberg T. B., Garrison-Kimmel S., Kupfer T., Sanderson R. E., 2019, MNRAS, 490, 5888
Li W., Chornock R., Leaman J., Filippenko A. V., Poznanski D., Wang X., Ganeshalingam M., Mannucci F., 2011, MNRAS, 412, 1473
Li Z., Chen X., Ge H., Chen H.-L., Han Z., 2023, A&A, 669, A82
Liu Z.-W., Röpke F. K., Han Z., 2023, Research in Astronomy and Astrophysics, 23, 082001
Livio M., Soker N., 1988, ApJ, 329, 764
Livne E., 1990, ApJ, 354, L53
Lomb N. R., 1976, Ap&SS, 39, 447
Luo C., et al., 2024, arXiv e-prints, p. arXiv:2404.04835
Maoz D., Mannucci F., 2012, Publ. Astron. Soc. Australia, 29, 447
Maoz D., Mannucci F., Nelemans G., 2014, ARA&A, 52, 107
Marsh T. R., 1989, PASP, 101, 1032
Marsh T. R., 2011, Classical and Quantum Gravity, 28, 094019
Marsh T., 2019, molly: 1D astronomical spectra analyzer, Astrophysics Source Code Library, record ascl:1907.012 (ascl:1907.012)
Marsh T. R., Nelemans G., Steeghs D., 2004, MNRAS, 350, 113
Maxted P. F. L., Marsh T. R., North R. C., 2000, MNRAS, 317, L41
Maxted P. F. L., Marsh T. R., Moran C. K. J., 2002, MNRAS, 332, 745
Munday J., 2024, JamesMunday98/WD-BASS: v1.0.0, doi:10.5281/zenodo.11188044, https://doi.org/10.5281/zenodo.11188044
Munday J., et al., 2023, MNRAS, 518, 5123
Munday J., et al., 2024, MNRAS, 532, 2534
Nelemans G., Verbunt F., Yungelson L. R., Portegies Zwart S. F., 2000, A&A, 360, 1011
Nelemans G., Yungelson L. R., Portegies Zwart S. F., Verbunt F., 2001, A&A, 365, 491
Nelemans G., et al., 2005, A&A, 440, 1087
Nugent P. E., et al., 2011, Nature, 480, 344
O'Brien M. W., et al., 2024, MNRAS, 527, 8687
Pakmor R., Edelmann P., Röpke F. K., Hillebrandt W., 2012, MNRAS, 424, 2222
Pakmor R., Kromer M., Taubenberger S., Springel V., 2013, ApJ, 770, L8
Pakmor R., Springel V., Bauer A., Mocz P., Munoz D. J., Ohlmann S. T., Schaal K., Zhu C., 2016, MNRAS, 455, 1134
Pakmor R., Zenati Y., Perets H. B., Toonen S., 2021, MNRAS, 503, 4734
Pakmor R., et al., 2022, MNRAS, 517, 5260
Pakmor R., Seitenzahl I. R., Ruiter A. J., Sim S. A., Röpke F. K., Taubenberger S., Bieri R., Blondin S., 2024, A&A, 686, A227
Pan T., Kasen D., Loeb A., 2012, MNRAS, 422, 2701
Paxton B., Bildsten L., Dotter A., Herwig F., Lesaffre P., Timmes F., 2011, ApJS, 192, 3
Paxton B., et al., 2013, ApJS, 208, 4
Paxton B., et al., 2015, ApJS, 220, 15
Paxton B., et al., 2018, ApJS, 234, 34
Paxton B., et al., 2019, ApJS, 243, 10
Pelisoli I., et al., 2021, Nature Astronomy, 5, 1052
Peters P. C., 1964, Physical Review, 136, 1224
Postnov K. A., Yungelson L. R., 2014, Living Reviews in Relativity, 17, 3
Prochaska J., et al., 2020, The Journal of Open Source Software, 5, 2308
Rebassa-Mansergas A., Parsons S. G., García-Berro E., Gänsicke B. T., Schreiber M. R., Rybicka M., Koester D., 2017, MNRAS, 466, 1575
Rebassa-Mansergas A., Toonen S., Korol V., Torres S., 2019, MNRAS, 482, 3656
Ren L., Li C., Ma B., Cheng S., Huang S.-J., Tang B., Hu Y.-m., 2023, ApJS, 264, 39
Ricker G. R., et al., 2015, Journal of Astronomical Telescopes, Instruments, and Systems, 1, 014003
Sahu S., et al., 2023, MNRAS, 526, 5800
Scargle J. D., 1982, ApJ, 263, 835
Seitenzahl I. R., Meakin C. A., Townsley D. M., Lamb D. Q., Truran J. W., 2009, ApJ, 696, 515
Shen K. J., Bildsten L., 2014, ApJ, 785, 61
Shen K. J., Boos S. J., Townsley D. M., Kasen D., 2021, ApJ, 922, 68
Shen K. J., Boos S. J., Townsley D. M., 2024, arXiv e-prints, p. arXiv:2405.19417
Sim S. A., 2007, MNRAS, 375, 154
Sim S. A., Röpke F. K., Hillebrandt W., Kromer M., Pakmor R., Fink M., Ruiter A. J., Seitenzahl I. R., 2010, ApJ, 714, L52
Soker N., 2024, The Open Journal of Astrophysics, 7, 31
Springel V., 2010, MNRAS, 401, 791
Temmink K. D., Pols O. R., Justham S., Istrate A. G., Toonen S., 2023, A&A, 669, A45
Thorne K. S., 1980, Reviews of Modern Physics, 52, 299
Toonen S., Nelemans G., Portegies Zwart S., 2012, A&A, 546, A70
Toonen S., Hollands M., Gänsicke B. T., Boekholt T., 2017, A&A, 602, A16
Tremblay P. E., Gianninas A., Kilic M., Ludwig H. G., Steffen M., Freytag B., Hermes J. J., 2015, ApJ, 809, 148
Webbink R. F., 1984, ApJ, 277, 355
Weinberger R., Springel V., Pakmor R., 2020, ApJS, 248, 32
Whitmore J. B., Murphy M. T., 2015, MNRAS, 447, 446

Table A1. A table of all observed RVs (without relativistic correction) and the mid-exposure time-stamps. Wavelength calibration errors were propagated.

HJD−2450000 UTC	RV_1 [km s^{-1}]	ΔRV_1 [km s^{-1}]	RV_2 [km s^{-1}]	ΔRV_2 [km s^{-1}]	Source
8588.734699	−43.83	10.22	128.60	10.26	ISIS
8588.739403	−48.34	13.12	126.60	7.82	ISIS
8591.687642	−47.74	4.63	137.97	3.93	ISIS
8591.698183	−42.98	5.32	139.73	4.46	ISIS
8591.745818	−24.42	4.93	117.45	7.48	ISIS
8591.752887	−13.34	3.91	113.95	4.84	ISIS
8645.660736	−46.33	4.10	139.79	3.97	ISIS
8645.670120	−41.48	4.08	139.02	3.52	ISIS
8731.364001	149.73	9.28	−27.17	13.79	IDS
8732.411857	95.08	11.14	23.01	11.46	IDS
8732.432828	112.69	14.73	13.43	19.28	IDS
8732.460152	146.81	5.43	−24.69	8.03	IDS
8732.481127	137.36	9.86	−21.20	12.24	IDS
8732.506595	139.55	7.35	−18.77	3.99	IDS
8733.496923	−13.87	9.40	110.97	8.23	IDS
8733.517893	13.12	11.25	103.55	11.63	IDS
8734.382747	136.13	10.99	1.58	10.44	IDS
8751.390254	124.27	25.16	15.48	35.06	IDS
8751.400810	75.08	31.95	39.30	22.87	IDS
8751.411366	111.57	19.70	24.70	35.63	IDS
8751.421919	103.05	36.85	13.66	29.44	IDS
10385.714514	121.92	11.34	−48.04	5.86	FIES
10389.693347	95.12	3.91	−14.90	19.24	FIES
10389.711256	100.95	8.79	−19.22	14.96	FIES
10401.639249	137.53	4.08	−30.59	2.21	FIES
10401.675067	137.67	5.83	−44.11	3.54	FIES
10401.692976	149.54	12.12	−50.05	8.55	FIES
10402.602016	−40.56	10.65	122.89	4.08	FIES
10403.596407	23.18	18.31	56.32	4.86	FIES
10405.726945	119.48	6.67	−14.62	6.83	FIES
10412.657048	−25.61	7.60	146.64	4.69	FIES
10416.579027	123.96	6.33	−18.52	6.26	FIES
10426.543453	135.26	12.18	−39.47	8.71	IDS
10426.561527	155.21	6.64	−32.92	5.31	IDS
10426.579516	147.89	8.65	−51.49	5.29	IDS
10426.597579	150.34	8.63	−53.96	7.91	IDS
10426.615569	142.23	8.13	−36.32	5.93	IDS
10426.633728	141.73	10.30	−27.52	5.79	IDS
10426.651797	121.16	10.04	−22.66	9.27	IDS
10426.675840	104.72	6.37	3.20	4.94	IDS
10426.693911	99.42	18.86	10.39	9.92	IDS

Table A1. continued...

HJD−2450000 UTC	RV_1 [km s^{-1}]	ΔRV_1 [km s^{-1}]	RV_2 [km s^{-1}]	ΔRV_2 [km s^{-1}]	Source
10426.711986	60.03	9.14	41.66	9.22	IDS
10426.730069	55.33	4.57	54.96	3.95	IDS
10427.568303	22.90	13.36	98.97	12.29	IDS
10427.586293	38.01	10.43	82.12	10.65	IDS
10427.604333	52.56	13.10	63.98	7.18	IDS
10427.640501	78.96	10.17	37.00	5.90	IDS
10427.658595	80.16	9.54	2.07	10.28	IDS
10427.677213	111.05	6.78	−2.50	9.76	IDS
10427.695279	119.40	9.22	−15.23	5.24	IDS
10427.713363	129.54	14.44	−16.45	9.41	IDS
10435.613760	56.04	4.41	55.55	3.10	FIES
10451.692321	5.16	4.73	83.75	7.77	FIES
10451.710229	−3.64	4.86	117.82	3.49	FIES
10462.684526	126.24	5.78	−20.07	5.89	ALFOSC
10463.515200	57.13	6.48	60.23	3.75	ALFOSC
10463.522815	53.00	8.06	57.95	5.32	ALFOSC
10463.530392	42.85	7.76	82.97	8.49	ALFOSC
10463.613866	−30.69	6.79	150.23	15.31	ALFOSC
10471.660727	142.69	1.09	−44.14	0.80	UVES
10471.669856	145.29	0.81	−44.88	0.94	UVES
10471.678957	143.42	1.04	−40.03	0.71	UVES
10471.688045	141.58	1.02	−37.81	0.75	UVES
10471.697140	136.39	1.12	−32.99	0.98	UVES
10471.706232	135.55	0.93	−26.67	0.93	UVES
10471.715322	129.76	1.02	−24.49	0.93	UVES
10471.724414	122.58	1.17	−16.54	0.89	UVES
10471.733505	117.61	1.09	−14.89	0.85	UVES
10471.742600	106.43	1.07	−4.46	0.97	UVES
10471.751691	104.14	1.27	3.99	0.94	UVES
10471.760789	94.76	1.39	12.92	0.94	UVES
10471.769880	84.35	1.31	18.86	0.92	UVES
10471.778969	79.40	2.45	30.92	2.07	UVES
10471.788065	67.00	4.46	40.27	6.17	UVES
10471.797156	62.90	3.46	48.17	1.98	UVES
10471.806251	56.81	11.41	56.94	16.47	UVES
10471.815355	48.61	7.41	60.71	9.05	UVES
10471.824448	37.51	8.51	72.91	6.31	UVES
10471.833536	27.02	1.78	80.67	2.15	UVES
10525.451278	60.95	5.62	60.27	3.17	FIES
10525.469185	57.98	3.66	63.47	4.66	FIES
10545.435565	−33.32	6.71	131.51	4.64	FIES

Whitmore J. B., Murphy M. T., Griest K., 2010, ApJ, 723, 89
Willems B., Kolb U., 2004, A&A, 419, 1057
Woods T. E., Ivanova N., van der Sluys M. V., Chaichenets S., 2012, ApJ, 744, 12
van der Sluys M. V., Verbunt F., Pols O. R., 2006, A&A, 460, 209

APPENDIX A: RADIAL VELOCITY MEASUREMENTS

This paper has been typeset from a TEX/LATEX file prepared by the author.